Solar Wind-Magnetosphere Coupling During Radial Interplanetary Magnetic Field Conditions: Simultaneous Multi-Point Observations

S Toledo-redondo, K.-J. Hwang, C P Escoubet, B Lavraud, J Fornieles, N Aunai, R C Fear, J Dargent, H. S Fu, S. A. Fuselier, et al.

JGR Space Physics

RESEARCH ARTICLE
10.1029/2021JA029506

Special Section:
Cluster 20th anniversary: results from the first 3D mission

Solar Wind—Magnetosphere Coupling During Radial Interplanetary Magnetic Field Conditions: Simultaneous Multi-Point Observations

S. Toledo-Redondo[1,2], K.-J. Hwang[3], C. P. Escoubet[4], B. Lavraud[5,2], J. Fornieles[6], N. Aunai[7], R. C. Fear[8], J. Dargent[9], H. S. Fu[10], S. A. Fuselier[3,11], K. J. Genestreti[12], Yu V. Khotyaintsev[13], W. Y. Li[14], C. Norgren[15], and T. D. Phan[16]

[1]Department of Electromagnetism and Electronics, University of Murcia, Murcia, Spain, [2]Institut de Recherche en Astrophysique et Planétologie, Université de Toulouse, CNRS, UPS, CNES, Toulouse, France, [3]Southwest Research Institute, San Antonio, TX, USA, [4]ESA, European Space Research and Technology Centre, Noordwijk, Netherlands, [5]Laboratoire d'Astrophysique de Bordeaux, Univ. Bordeaux, CNRS, Pessac, France, [6]Department of Electromagnetism and Matter Physics, University of Granada, Granada, Spain, [7]UMR7648 Laboratoire de physique des plasmas (LPP), Palaiseau, France, [8]School of Physics and Astronomy, University of Southampton, Southampton, UK, [9]Institut für Theoretische Physik, Ruhr-Universität Bochum, Bochum, Germany, [10]School of Space and Environment, Beihang University, Beijing, China, [11]Department of Physics and Astronomy, University of Texas at San Antonio, San Antonio, TX, USA, [12]Southwest Research Institute, Durham, NH, USA, [13]Swedish Institute of Space Physics, Uppsala, Sweden, [14]State Key Laboratory of Space Weather, National Space Science Center, Chinese Academy of Sciences, Beijing, China, [15]University of Bergen, Bergen, Norway, [16]SSL, University of California, Berkeley, CA, USA

Key Points:

- Simultaneous observations of the equatorial subsolar magnetopause and dusk flank during time-extended radial interplanetary magnetic field
- The magnetosphere enlarges ~0.7 R_E in the subsolar region but <0.2 R_E in the flank due to the reduced pressure exerted by the solar wind
- Simultaneous reconnection evidence in the subsolar and flank regions more than 15 R_E apart is observed during part of the encounter

Supporting Information:

Supporting Information may be found in the online version of this article.

Correspondence to:

S. Toledo-Redondo,
sergio.toledo@um.es

Citation:

Toledo-Redondo, S., Hwang, K.-J., Escoubet, C. P., Lavraud, B., Fornieles, J., Aunai, N., et al. (2021). Solar wind—Magnetosphere coupling during radial interplanetary magnetic field conditions: Simultaneous multi-point observations. *Journal of Geophysical Research: Space Physics*, *126*, e2021JA029506. https://doi.org/10.1029/2021JA029506

Received 29 APR 2021
Accepted 26 OCT 2021

Abstract In-situ spacecraft missions are powerful assets to study processes that occur in space plasmas. One of their main limitations, however, is extrapolating such local measurements to the global scales of the system. To overcome this problem at least partially, multi-point measurements can be used. There are several multi-spacecraft missions currently operating in the Earth's magnetosphere, and the simultaneous use of the data collected by them provides new insights into the large-scale properties and evolution of magnetospheric plasma processes. In this work, we focus on studying the Earth's magnetopause (MP) using a conjunction between the Magnetospheric Multiscale and Cluster fleets, when both missions skimmed the MP for several hours at distant locations during radial interplanetary magnetic field (IMF) conditions. The observed MP positions as a function of the evolving solar wind conditions are compared to model predictions of the MP. We observe an inflation of the magnetosphere (~0.7 R_E), consistent with magnetosheath pressure decrease during radial IMF conditions, which is less pronounced on the flank (<0.2 R_E). There is observational evidence of magnetic reconnection in the subsolar region for the whole encounter, and in the dusk flank for the last portion of the encounter, suggesting that reconnection was extending more than 15 R_E. However, reconnection jets were not always observed, suggesting that reconnection was patchy, intermittent or both. Shear flows reduce the reconnection rate up to ~30% in the dusk flank according to predictions, and the plasma β enhancement in the magnetosheath during radial IMF favors reconnection suppression by the diamagnetic drift.

1. Introduction

The Earth's magnetopause (MP) is the boundary between the Earth's magnetosphere, dominated by the Earth's intrinsic magnetic field, and the shocked solar wind, i.e., the magnetosheath, dominated by the Sun's intrinsic magnetic field. Magnetic reconnection and the Kelvin-Helmholtz instability take place at the MP, and are believed to be the two major coupling mechanisms between the magnetosphere and the solar wind, enabling energy and particle exchange between the two regions. To study the MP using in-situ instrumentation one needs to know where it is located in space as a function of time. Its location and shape depends mainly on upstream solar wind conditions, and the MP has been subject of study during the last decades, both using numerical simulations (e.g., Lu et al., 2011, 2013; Palmroth et al., 2001; Wiltberger et al., 2003) and empirical models built from in-situ spacecraft observations (e.g., Boardsen et al., 2000; Dusik et al., 2010; Fairfield, 1971; Lin et al., 2010; Petrinec & Russell, 1996; Safrankova et al., 2002; Shue et al., 1998; Sibeck et al., 1991; Wang et al., 2013).

The model reported by Shue et al. (1998) (S98) is a widely used MP model, based on 553 MP crossings. It uses a simple analytical form and assumes a symmetric MP around the GSE X-axis. It depends on two parameters: the solar wind dynamic pressure (P_d) and the magnitude of the Z-component of the interplanetary magnetic field (IMF) (B_z). Its functional form is

$$r = r_0\left(\frac{2}{1+\cos\theta}\right)^{\alpha} \quad (1)$$

where r is the radial distance to the Earth's center, and θ is the solar zenith angle. α and r_0 are found empirically as a function of IMF B_z and solar wind dynamic pressure. The predictions of this model are similar to the predictions by Petrinec and Russell (1996) (PR96), another widely used axisymmetric model. Case and Wild (2013) estimated, using more than 2,700 crossings of the Cluster spacecraft (polar orbit), spanning more than 8 years, that on average these two models tend to overestimate the radial distance between the MP and the Earth center by ~1 R_E (9%).

Since the S98 and PR96 models are axisymmetric, they cannot account for cusp indentations, and are expected to produce deviations at high latitudes. The model reported by Lin et al. (2010) (L2010) is another empirical model, where the asymmetry of the MP and the effect of the dipole tilt are considered. As additional inputs, it uses the IMF magnetic pressure (P_m) and the dipole tilt (Φ). They employed 2,708 MP crossings from multiple spacecraft to build their model, which uses 21 free parameters. Case and Wild (2013) estimated, using the same database mentioned above, that the radial MP distance was underestimated, on average, by ~0.25 R_E (2.3%). Other non-axisymmetric models present in the literature are, for instance, Boardsen et al. (2000) and Wang et al. (2013).

Samsonov et al. (2016) performed an exhaustive model comparison, including eight empirical models and seven MHD models. They concluded that empirical models yield differences in radial distance of the order of 1 R_E between themselves. Depending on the solar wind upstream conditions, different models may provide better predictions than others, whose accuracy also depends on the MP latitude. For instance, the L10 model provides the best predictions for the case $B_z = 0$, and these predictions are very close to MHD models. They also noted that none of the models is designed to account for radial IMF conditions, when the MP location drifts toward the Sun (D. Fairfield et al., 1990; Merka et al., 2003).

Radial IMF conditions (IMF cone angles <25° or >155°), represent ~15% of observations at 1 AU (Pi et al., 2014; Suvorova et al., 2010), although they have received much less attention than northward and southward IMF conditions. For radial IMF, a quasi-parallel bow shock in the subsolar region is formed, resulting in lower magnetic pressure exerted on the magnetosphere. In addition, the dynamic pressure of the solar wind is usually small for radial IMF (P_d < 1.5 nPa) (e.g., Park et al., 2016), plus the magnetosheath dynamic pressure becomes even smaller than in the solar wind, partly due the increase of reflected ions in the quasi-parallel bow shock. Therefore, the total pressure that the magnetosphere experiences is much smaller than for IMF cone angles close to 90°, and as a result the MP expands toward the Sun. Merka et al. (2003), based on a two-point MP observation event, proposed a bullet-shaped expansion of the magnetosphere for radial IMF, featuring an expansion toward the Sun in the subsolar region and thinning in the flanks. By contrast, Dusik et al. (2010) proposed a global expansion of the magnetosphere during radial IMF, featuring an inflation both in the subsolar region and in the flanks, based on statistical observations (~6,500 MP crossings from THEMIS) during radial IMF.

Dusik et al. (2010) also reported that the PR96 empirical model tends to underestimate the radial position of the MP, in particular when the IMF has a large radial component, from ~0.3 R_E for cone angle of 90° to ~1.7 R_E for cone angle close to 0° or 180°. They attributed it to a decrease in the effective dynamic pressure exerted at the boundary. Samsonov et al. (2012) studied the effective total pressure reduction over the MP using MHD simulations and THEMIS observations. They concluded that the total pressure exerted near the subsolar MP is reduced by ~24% when the IMF cone angle is close to 0° or 180°. Suvorova and Dmitriev (2015) compared various MP models and concluded that for low solar wind dynamic pressure conditions (P_d < 0.3 nPa), typical of radial IMF conditions, L2010 model performed better than S98 and PR96 models, although none of these models could account for the magnetosheath P_d reduction with respect to P_d in the solar wind for radial IMF.

The coupling between the Earth's magnetosphere and the solar wind is largely controlled by magnetic reconnection, which is most efficient during southward IMF conditions, i.e., the magnetic flux density reconnected per unit time maximizes. The amount of energy transferred to the Earth's magnetosphere system depends on the efficiency of this coupling, which is governed by both the reconnection rate and the extent of the X line. Cassak and Shay (2007) found scaling relations of the reconnection rate for asymmetric reconnection, which have been tested both using numerical simulations and statistical observations. The denser magnetosheath dominates the hybrid Alfvén velocity and controls, to a large extent, the reconnection rate (e.g., Borovsky, 2008; Borovsky et al., 2013; Lavraud & Borovsky, 2008; Fuselier et al., 2017). In the presence of cold ions of ionospheric origin, the outer dayside magnetosphere sometimes can have densities similar to magnetosheath densities, which also impact the reconnection rate (Borovsky & Denton, 2006; Dargent et al., 2020; Fuselier, Mukherjee, et al., 2019; Fuselier, Trattner, et al., 2019; Fuselier et al., 2021; Walsh et al., 2013).

The extent of the X line at the MP has been constrained using spacecraft conjunctions by a number of studies, most of them during southward IMF conditions. There have been various studies that made use of simultaneous multi-point observations during southward IMF, and have reported extended X line lengths at the MP, with measured minimum lengths ranging from two to nine Earth radii (R_E), and potentially extending longer distances (Berchem et al., 2008; Dunlop et al., 2011; Fear et al., 2009; Kitamura et al., 2016; Marchaudon et al., 2005; Phan et al., 2000). Similarly, Phan et al. (2006) reported an X line extending at least 8 R_E during B_y IMF. On the other hand, Walsh et al. (2017) used simultaneous (less than 1 min) observations of the MP on two THEMIS spacecraft separated by 3.9 Earth radii in the Y_{GSM} direction. They found signatures of reconnection (jets) only in one of the spacecraft, challenging the model of an extended X line as predicted by MHD global simulations. The situation they found is consistent with either spatially patchy reconnection or a spatially limited X line. Reconnection switching on and off in time is not consistent with their observations owing to the simultaneity of the measurements. The IMF was southward but the cone angle for this event was ∼50°.

Although what controls the extent of the X line at the MP is not fully understood, there are two mechanisms that are expected to suppress magnetic reconnection locally: shear flows and diamagnetic drifts along the reconnection jet direction. Cowley and Owen (1989) indicated that magnetic reconnection should be suppressed if the flow shear velocity parallel to the jet direction exceeds twice the Alfvén speed of the magnetosheath. La Belle-Hamer et al. (1995) suggested that twice the largest Alfvén speed (magnetosphere or magnetosheath) would be the critical speed for determining reconnecting suppression by shear flows. For symmetric reconnection, Cassak and Otto (2011) found that if the shear flow exceeds the Alfvén speed, reconnection is suppressed. Their simulations provided a scaling law for the reconnection rate

$$E \sim E_0 \left(1 - \frac{v_s^2}{v_A^2}\right), \tag{2}$$

where E and E_0 correspond to the reconnecting electric field with and without correction for the shear flow reduction, v_s is the shear flow speed in the outflow direction, and v_A is the Alfvén speed.

More recently, Doss et al. (2015) extended the formulation in Equation 2 to the case of asymmetric magnetic reconnection. They showed, using two-fluid simulations, that asymmetric reconnection may be more difficult to suppress by shear flows when the asymmetry is large, as it is the case at the MP:

$$E_{asym} \sim E_{0,asym} \left(1 - \frac{v_s^2}{v_{A,asym}^2} \frac{4\rho_1 B_2 \rho_2 B_1}{(\rho_1 B_2 + \rho_2 B_1)^2}\right), \tag{3}$$

where E_{asym} and $E_{0,asym}$ correspond to the resulting reconnecting electric field with and without correction for the shear flow in asymmetric reconnection, $v_{A,asym}$ is the hybrid Alfvén speed (Cassak & Shay, 2007), ρ is the mass density, B is the magnetic field strength, and subscripts 1 and 2 stand for each region adjacent to the reconnecting current sheet. This prediction has been shown to hold in particle-in-cell simulations (CDoss et al., 2016). Equation 3 may have implications for our current understanding on how planetary magnetospheres interact with the solar wind. For instance in Saturn, shear flow suppression has been

considered a major suppression mechanism by e.g., Desroche et al. (2013). However, Sawyer et al. (2019) did not find evidence of reconnection suppression by shear flows at Saturn.

Another mechanism that is known to be able to suppress magnetic reconnection is the diamagnetic drift of the reconnection X line (along the outflow direction) due to pressure gradients across the current sheet. The condition for reconnection suppression is that the diamagnetic drift speed exceeds the Alfvén velocity (Swisdak et al., 2003, 2010). This suppression condition is often expressed as

$$\Delta\beta > 2(L/d_i)\tan(\theta/2), \tag{4}$$

where $\Delta\beta$ is the change in plasma β across the current sheet, L is the current sheet width, d_i is the ion skin depth and θ is the magnetic field shear angle across the current sheet at the reconnection site. Vernisse et al. (2020) noted that, strictly speaking, $\Delta\beta$ should be calculated using only the normal to the current sheet component of the pressure tensor (P_{nn} in LMN coordinates) and the guide field component of the magnetic field (B_M in LMN coordinates), although typically the total plasma β is considered. Studying this suppression mechanism is important because it has implications for how long the reconnection X line can be at the MP, for instance. It also indicates which magnetosheath conditions are less favorable for reconnection to take place. Tests of reconnection suppression by the diamagnetic drift at the MP of Earth (Phan et al., 2013) and Saturn (S. Fuselier et al., 2020) have been largely successful. Equation 4 indicates that this suppression mechanism is at work mainly for large guide field configurations or large β asymmetries in the plasma inflow.

In this work, we make use of quasi simultaneous observations of the MP near the subsolar region and the dusk flank. We first compare the actual location of the MP to various models and study its inflation and shape due to the reduced effective pressure exerted by the magnetosheath during radial IMF conditions. Using simultaneous crossings at distant regions allows us to observe the relative inflation in the two distant regions without the need of assumptions on the magnetosheath time evolution. Then, we study the occurrence of reconnection at each region and discuss our findings. This manuscript is organized as follows. In Section 2, we describe the magnetospheric multiscale (MMS) and Cluster orbits during the MP conjunction, its configuration and the main plasma properties during the event. In Section 3, we compare our observations to two model predictions of the MP location simultaneously in the flank and the subsolar region. In Section 4, we assess the occurrence of magnetic reconnection based on observations and compare it to the predictions of the reconnection suppression mechanisms. Finally, in Section 5, we discuss and summarize the main findings of this study.

2. Description of the MMS–Cluster MP Conjunctions on November 28, 2016

The Cluster mission (Escoubet et al., 2001) was launched in 2001 into an elliptical polar orbit with the aim of surveying multiple magnetospheric regions. It is composed of four identical spacecraft that have been flying in multiple configurations, e.g., tetrahedron or string of pearls, at different length-scales, from few km (electron scale) to several thousand km (MHD scale). In this work, we use measurements from the Flux-Gate magnetometer (Balogh et al., 1997), and Cluster Ion Spectrometry-Composition Distribution Function (CIS-CODIF) (Reme et al., 2001).

The MMS mission (Burch et al., 2015) was launched in 2015 with the aim of studying magnetic reconnection at the Earth's MP and magnetotail, with a focus on the associated kinetic-scale processes. It is a suite of four identical spacecraft flying in tetrahedron formation, to distinguish time from spatial variations. Each spacecraft has several instruments to measure plasma parameters. In this work, we use the flux gate magnetometers (Russell et al., 2014) and Fast Plasma Instrument (FPI) to measure electrons and ions (Pollock et al., 2016).

On November 28, 2016, both the Cluster and MMS fleets were skimming the MP simultaneously for several hours. Cluster was in the dusk flank near the terminator and MMS was near the subsolar region, at roughly (0, 15, 0) and (8, 5, 1) Earth radii (R_E) in GSE coordinates, respectively. The Cluster and MMS position in the interval 09:00–18:00 UT is shown in Figures 1a–1c, in the GSE XZ, XY, and YZ planes, respectively. $C1$ and $C2$ were at 0.5 R_E of separation and C3 and C4 at 0.4 R_E of separation, and the distance between the two groups was of ∼1.1 R_E. On the other hand, all four MMS spacecraft were in close (∼10 km) tetrahedron

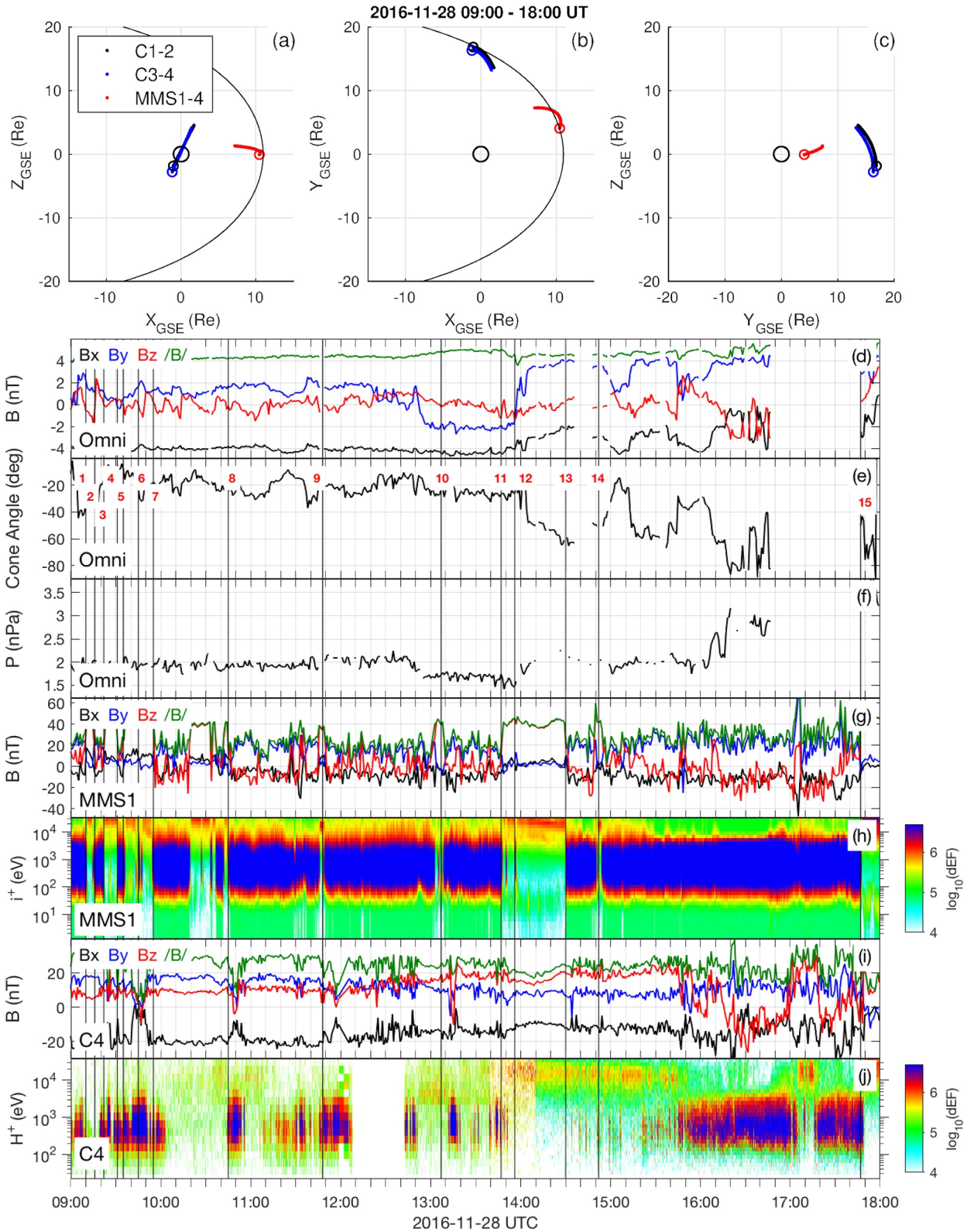
2016-11-28 09:00 - 18:00 UT
(a)
(b)
(c)
C1-2
C3-4
MMS1-4
Z_{GSE} (Re)
X_{GSE} (Re)
Y_{GSE} (Re)
(d)
Bx By Bz /B/
B (nT)
Omni
(e)
Cone Angle (deg)
(f)
P (nPa)
(g)
MMS1
(h)
i^+ (eV)
$\log_{10}$(dEF)
(i)
C4
(j)
H^+ (eV)
09:00
10:00
11:00
12:00
13:00
14:00
15:00
16:00
17:00
18:00
2016-11-28 UTC

Figure 1.

formation. For the rest of this work, all MMS measurements are taken from MMS1 and are representative of the other MMS spacecraft observations. During the MMS-Cluster conjunction studied here, the solar wind speed was roughly 400 km/s (not shown), and the IMF was dominated by GSE X component ($\mathbf{B}_{IMF} \simeq B_x$, Figures 1d and 1e). The solar wind conditions remained roughly stable between 09:00 - 14:00 UT. After that time, there is a **B** field rotation in Y and the dynamic pressure started increasing, from ∼1.5 nPa at 14:00 UT to more than 3 nPa at 18:00UT (Figure 1f), and the IMF cone angle (θ_{CA}) started fluctuating.

The next two panels show an overview of the observations made by MMS. Figure 1g shows MMS measured magnetic field in GSE coordinates. When MMS is in the magnetosphere, near the subsolar region, **B** is dominated by $B_z \simeq 40$ nT. Figure 1h shows the FPI ion omnidirectional spectrogram observed by MMS. The magnetosphere regions show high-energy ions at several keV, corresponding to the dayside plasma sheet population. A cold ion component of ionospheric origin is also detected by FPI most of the time in the magnetosphere, at few tens of eV (visible between 14:00 - 14:30 UT in Figure 1h). In the magnetosheath, the ion energies are of the order of several hundred eV to few keV. Figure 1i shows **B** field measurements in the dusk flank from C4 during the same time interval. B_z is positive at times when Cluster is in the magnetosphere, and $B_m \simeq 30$ nT, where subscript m stands for magnetosphere. Figure 1j shows the CODIF H^+ omnidirectional spectrogram measured by C4. It corresponds to the unique ion measurement available on the cluster fleet during the conjunction. The magnetospheric plasma sheet ion population, with energies above 10 keV, shows similar density and temperature in the flank (Cluster) and in the subsolar region (MMS). The magnetosheath ion population, on the other hand, shows lower density in the flank (not shown). Vertical black lines correspond to the times when a conjunction between any of the Cluster and MMS spacecraft was identified. We define the conjunctions when both the MMS fleet and at least one of the Cluster spacecraft cross the MP current sheet within an interval of less than 5 min. Using this criterion, we identify 15 conjunctions that are summarized in Table 1, corresponding to red numbers and vertical black lines in Figure 1e. Some of the conjunctions correspond to full crossings and some to partial crossings. Some of them are clean, single crossings, but others may correspond to multiple crossings within a short (less than 5 min) time interval.

3. Location and Shape of the MP

The observations of the MP reported in Table 1 allow us to test current models of the MP simultaneously at distant locations. We focus on two empirical models: S98 (Shue et al., 1998) and L10 (Lin et al., 2010). These models do not depend on IMF cone angle, and to account for the effect of the extended radial IMF observed during the conjunction, we use the effective magnetosheath pressure reduction reported by Samsonov et al. (2012), scaled linearly as a function of the IMF cone angle (θ_{CA}):

$$P_{d,sheath} = (0.76 + 0.121\theta_{CA})P_{d,SW}, \tag{5}$$

where θ_{CA} varies between 0 - $\pi/2$. This reduction in pressure was estimated using observations near the subsolar MP, with most data points fulfilling the condition $\sqrt{Y^2 + Z^2} < 10\ R_E$. In the following, we compare the two MP models with and without applying this correction (subscript c and no subscript, respectively), to test these results simultaneously both in the subsolar region and in the flank.

Table 2 shows the upstream solar wind conditions from the OMNI database, i.e., propagated to the bow shock (P_d, B_z, B_x/B) and the value of the dipole tilt (Φ) for the 15 crossings reported in Table 1. The magnetic pressure P_m is negligible (i.e., lower than 0.1 nPa) for all the events. OMNI makes use of the Advanced Composition Explorer (ACE) magnetometer (Smith et al., 1998) and ion detector (McComas et al., 1998) for inferring the solar wind parameters mentioned above. Based on the noise figures provided for the magnetometer, the uncertainty in the magnetic field-derived quantities (P_m, B_z, B_x/B) is less than 1%. For the dynamic pressure (P_d), we consider it is comparable to the energy resolution of the ion instrument, that

Figure 1. Overview of the November 28, 2016 magnetospheric multiscale–cluster magnetopause conjunction. (a) Spacecraft orbits, XZ GSE plane. (b) Spacecraft orbits, XY GSE plane. (c) Spacecraft orbits, YZ GSE plane. (d) Solar wind magnetic field in GSE coordinates (omni database). (e) IMF cone angle (omni database). (f) Solar wind dynamic pressure (omni database). (g) MMS magnetic field in GSE coordinates. (h) MMS FPI ion spectrogram in differential Energy Flux units (dEF), keV/(cm^2 s sr keV). (i) C4 magnetic field in GSE coordinates (j) C4 CODIF proton spectrogram in differential Energy Flux units (dEF), keV/(cm^2 s sr keV). Black vertical lines correspond to the occurrence times of events 1–15 in Table 1.

Table 1
Simultaneous (~5 min) Magnetospheric Multiscale and Cluster Magnetopause Crossings

	MMS 1–4			Cluster 1–2			Cluster 3–4		
ID	Time (UT)	Position[a] (GSE R_E)	B rotation[b]	Time (UT)	Position[a] (GSE R_E)	B rotation[b]	Time (UT)	Position[a] (GSE R_E)	B rotation[b]
1	09:10	10.5, 4.2, 0.0	full S-M	09:13	−1.0, 16.8, −1.7	full S-M	-	-	-
2	09:16	10.5, 4.2, 0.0	full M-S	09:20	−1.0, 16.8, −1.7	full M-S	09:20	−1.1, 16.3, −2.6	partial M-S-M
3	09:22	10.5, 4.3, 0.0	full S-M	-	-	-	09:25	−1.1, 16.3, −2.5	full M-S-M
4	09:31	10.6, 4.4, 0.0	full M-S	-	-	-	09:31	−1.0, 16.3, −2.4	partial M-S-M
5	09:35	10.6, 4.4, 0.0	full S-M	-	-	-	09:41	−1.0, 16.3, −2.4	full M-S
6	09:45	10.6, 4.5, 0.1	full M-S-M	-	-	-	09:51	−1.0, 16.3, −2.2	full S-M
7	09:55	10.6, 4.6, 0.1	full M-S	-	-	-	09:53	−0.9, 16.3, −2.1	partial M-S-M
8	10:45	10.6, 5.2, 0.2	full M-S	10:43	−0.5, 16.7, −0.6	full M-S	10:47	−0.7, 16.2, −1.4	full M-S
9	11:48	10.5, 5.7, 0.4	full S-M-S	-	-	-	11:48	−0.4, 16.1, −0.6	full M-S
10	13:07	10.2, 6.3, 0.6	full S-M-S	13:12	0.3, 16.1, 1.1	full M-S?	13:13	0.0, 15.7, 0.4	full M-S-M
11	13:47	9.9, 6.6, 0.8	full S-M	13:50	0.5, 15.9, 1.6	?	13:45	0.2, 15.5, 1.0	full M-S-M
12	13:56	9.9, 6.6, 0.8	partial M-S-M	13:56	0.5, 15.8, 1.7	partial M-S-M	13:56	0.3, 15.5, 1.1	partial M-S-M
13	14:30	9.6, 6.8, 0.9	full M-S	14:34	0.7, 15.6, 2.1	full M-S	14:34	0.4, 15.2, 1.5	partial M-S-M
14	14:52	9.4, 6.9, 0.9	full S-M-S	14:52	0.8, 15.4, 2.4	full S-M-S	14:52	0.5, 15.1, 1.8	multiple partial
15	17:47	7.4, 7.3, 1.3	full S-M	17:50	1.7, 13.8, 4.4	full S-M	17:48	1.4, 13.4, 4.0	full S-M

[a]Position corresponds to mean values during a 50-s interval centered at the reference time. [b]Type of crossing, S stands for magnetosheath and MM stands for Magnetosphere.

Table 2
Distance to Magnetopause Models (R_E)

	SW parameters				Model deviation (subsolar)				Model deviation (flank)			
ID	P_d (nPa)	Φ (°)	B_z (nT)	B_x/B	S98 (R_E)	S98$_c$ (R_E)	L10 (R_E)	L10$_c$ (R_E)	S98 (R_E)	S98$_c$ (R_E)	L10 (R_E)	L10$_c$ (R_E)
1	1,8	−24,8	−0,6	−0,8	−0,7	−0,3	−0,5	0,1	−0,2	0,3	0,4	0,5
2	1,9	−24,5	−1,1	−0,9	−0,8	−0,4	−0,7	−0,1	−0,3	0,3	−0,5	0,3
3	1,8	−24,3	0,2	−1,0	−0,7	−0,2	−0,4	0,2	−0,2	0,4	0,2	0,7
4	1,9	−23,9	0,3	−1,0	−0,8	−0,4	−0,5	−0,2	−0,3	0,3	0,3	−0,5
5	1,8	−23,8	0,2	−1,0	−0,8	−0,3	−0,5	0,1	−0,2	0,3	0,2	0,6
6	1,8	−23,3	0,1	−0,9	−0,8	−0,4	−0,5	0,1	−0,2	0,4	−0,2	0,6
7	1,8	−22,9	0,5	−0,9	−0,9	−0,4	−0,6	0,1	−0,2	0,3	−0,2	0,5
8	1,8	−20,9	−0,1	−0,9	−1,0	−0,6	−0,7	−0,2	−0,1	0,4	−0,3	0,6
9	1,9	−18,3	0,1	−0,9	−1,2	−0,8	−1,0	−0,4	−0,3	0,2	−0,4	0,4
10	1,6	−15,5	−0,2	−0,9	−0,9	−0,5	−0,6	−0,1	0,1	0,7	−0,1	0,8
11	1,6	−14,3	−1,2	−0,9	−0,8	−0,4	−0,7	−0,2	0,2	0,8	−0,3	0,7
12	1,4	−14,1	−1,3	−0,9	−0,5	−0,1	−0,4	0,2	0,5	1,1	0,4	1,2
13	2,0	−13,3	−0,5	−0,6	−1,0	−0,7	−0,8	−0,5	−0,1	0,2	0,4	0,1
14	2,0	−12,8	0,7	−0,5	−0,8	−0,5	−0,7	−0,3	−0,1	0,2	−0,3	−0,2
15	3,2	−12,3	0,3	−0,6	0,1	0,3	−0,1	0,3	−0,3	−0,1	−0,8	−0,5

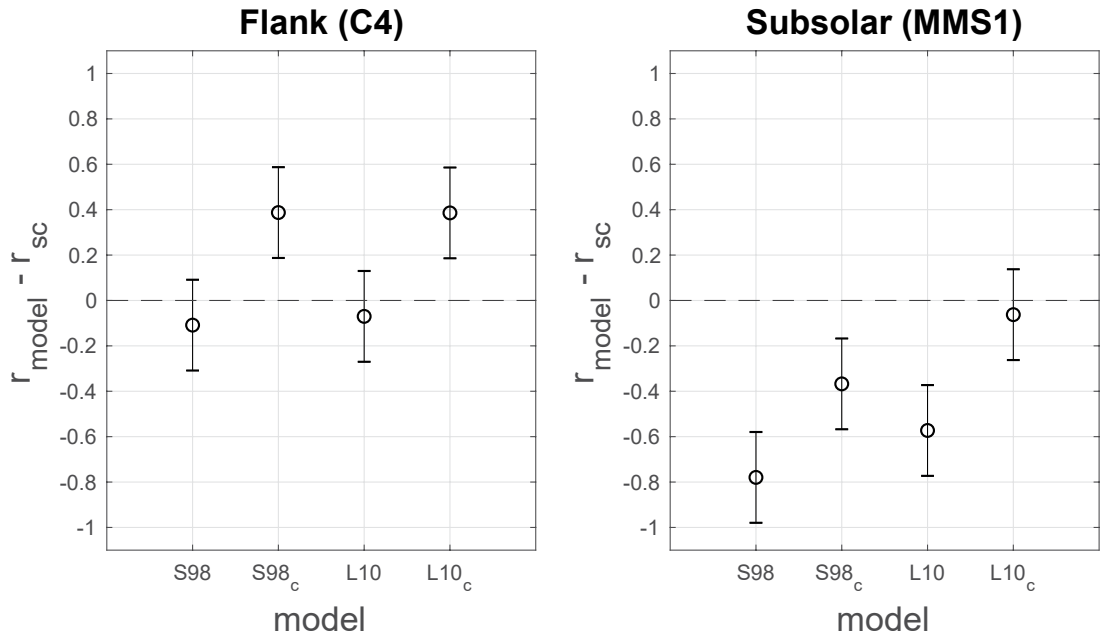

Figure 2. (left) Distance between the mean observed magnetopause (MP) position in the flank (r_{sc}), averaged over the 15 events of Table 1, and the MP model predictions (r_{model}). (right) Distance between the mean observed MP position in the subsolar region (r_{sc}), averaged over the 15 events of Table 1, and the MP model predictions (r_{model}). Error bars indicate ±0.2 R_E uncertainties, corresponding to 10% uncertainty in P_d measurement.

is 5%. These uncertainties in the solar wind parameters correspond to roughly ±0.1 R_E uncertainty in the model predictions of the MP position, both in the subsolar and flank regions (not shown). If we consider 10% uncertainty in the P_d measurement, the associated uncertainty of the models becomes roughly ±0.2 R_E. Using these input values, we computed the MP location for S98 and L10 models, with and without the correction defined in Equation 5 (subscript c for corrected pressure) suggested by Samsonov et al. (2012). Table 2 also shows the distance of MMS constellation and C4 to the MP models. A negative sign corresponds to $r_{model} < r_{sc}$. The distance between the observed location of the MP and the location predicted by each model are summarized in Figure 2. The mean distance over the 15 simultaneous crossings is plotted using circles, and the error bars correspond to ±0.2 R_E, i.e., 10% uncertainty in P_d. At the flank MP, both S98 and L10 match the measured MP position within the error bars. In the subsolar region, the models S98 and L10 underestimate the MP position by ∼0.8 R_E and ∼0.6 R_E on average, respectively, the corrected model $S98_c$ underestimates the MP position by ∼0.4 R_E and and $L10_c$ provides a correct estimate within the error bars. Therefore, the corrections for radial IMF yield better results in the subsolar region, with the model $L10_c$ as the most accurate one. On the other hand, the corrections for radial IMF in the flank overestimate the measured MP position by ∼0.4 R_E on average, while the models without correction provide accurate MP positions within the error bars. The corrections in the pressure exerted during radial IMF were obtained using spacecraft data near the subsolar region, and we confirm the validity of the calculations by reported by Samsonov et al. (2012) in that region. In addition, we note that these corrections cannot be extrapolated to the flanks.

Figure 3a shows the MMS (red) and C4 (blue) orbits during the 9-hr interval. Red and blue dots correspond to each of the 15 MP crossings of Tables 1 and 2 for MMS and C4, respectively. The black and green curves correspond to the S98 and L10 MP models corresponding to the solar wind conditions at the beginning of the time interval in Figure 1. Figures 3b–3g show details of crossings 2, 13 and 15 and the MP models for the solar wind conditions at the time of each event, for MMS (red) and C4 (blue).

4. Magnetic Reconnection at the Subsolar and Dusk Flank MP

Next, we take the events of Table 1 that have full MP crossings for both MMS and C4 (i.e., events 3, 5, 6, 8, 9, 10, 11, and 15) and apply minimum variance analysis (MVA) to the magnetic field. The N direction obtained in the subsolar region and in the flank is roughly consistent with the MP model predictions, except

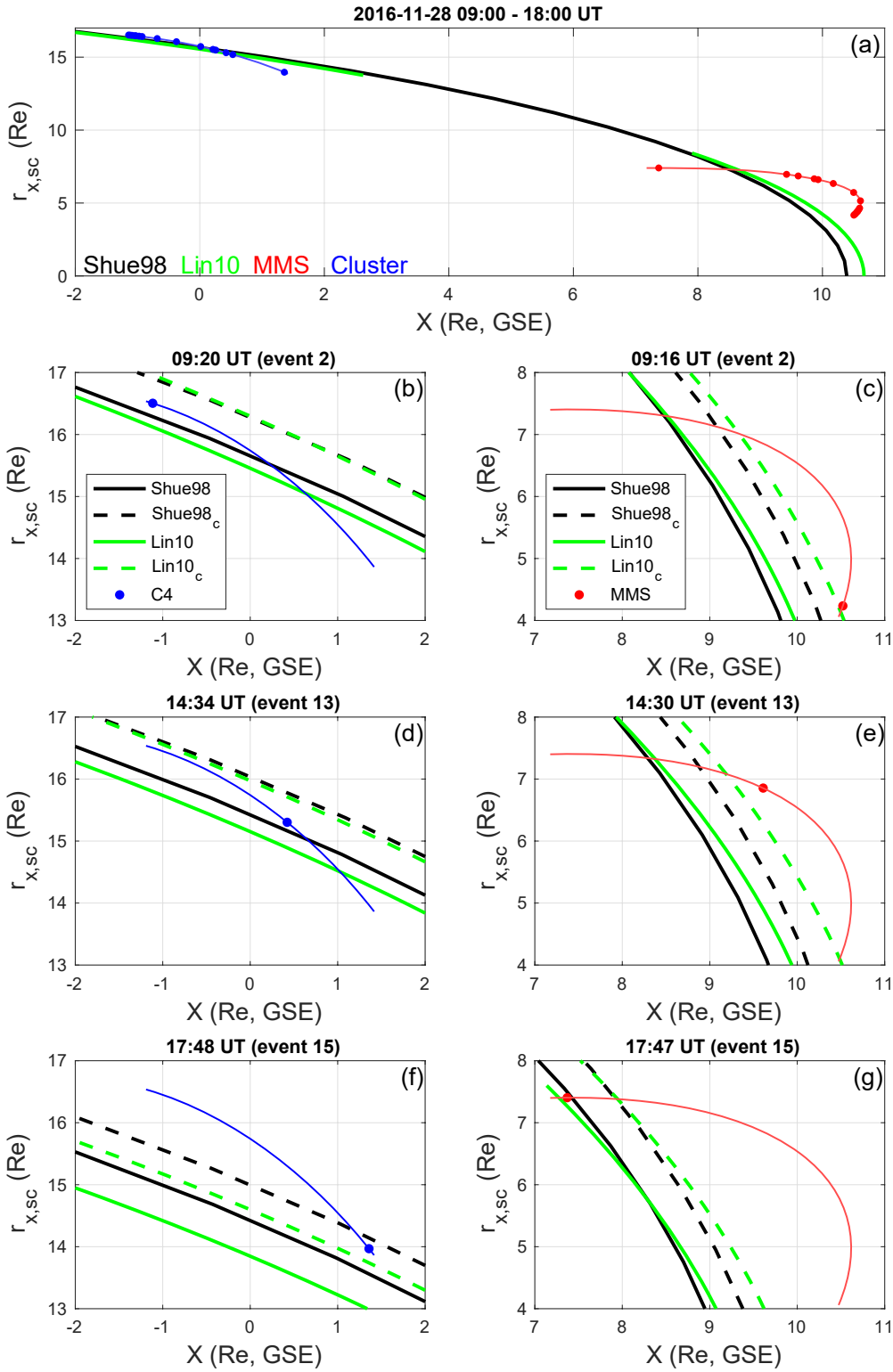

Figure 3. MP models estimation during the MMS-Cluster conjunction (November 28, 2016 09:00–18:00 UT). (a) C4 (blue) and MMS (red) orbits, the spacecraft position at the times indicated in Table 1 are marked using circles (Black) Reference S98 model and (green) reference L10 model. (b) Detail of the C4 position for event two in Table 1 (Solid) S98 and L10 models for nominal solar wind conditions and (dashed) for corrected solar wind conditions (Samsonov et al., 2012). (c) Detail of the MMS position for event two in Table 1 (Solid) S98 and L10 models for nominal solar wind conditions and (dashed) for corrected solar wind conditions (Samsonov et al., 2012). (d) Same as (b) for event 13 in Table 1. (e) Same as (c) for event 13 in Table 1. (f) Same as (b) for event 15 in Table 1. (g) Same as (c) for event 15 in Table 1.

for event 9, when the obtained *N*-direction at the subsolar region (MMS) is roughly in the *Z* GSE direction. This can be either to a poor performance of MVA (intermediate to minimum eigenvalue ratio is ∼3 for this case) or reconnection 3D effects. We find it difficult to interpret this event and it is discarded. For each of the non-discarded events, we search for observational evidence of ongoing reconnection based on two criteria: presence of reconnection jets in the *L* direction and the existence of electron only Low Latitude Boundary layer (eLLBL) earthward of the MP (Gosling et al., 1990). We also estimate and compare the conditions on both sides of the MP (magnetosphere, *sp*, and magnetosheath, *sh*) simultaneously in the subsolar region (MMS) and at the dusk flank (C4), which allow us to test the theoretical conditions for reconnection suppression discussed in the introduction (Equations 3 and 4).

Figure 4 shows an example (event 15) on how we proceeded to obtain LMN coordinates, search for reconnection signatures, and obtain the *sp* and *sh* conditions simultaneously in the subsolar region and in the flank. Panels a–e correspond to Cluster (C4) observations, and panels f–j correspond to MMS observations of the same variables, namely magnetic field, ion density, ion velocity, ion spectrogram and electron spectrogram. All vectors are provided in local LMN coordinates, obtained from applying MVA to the **B** field in the yellow-shaded regions, which correspond to the MP crossing. The LMN coordinates are specified in panels a and *f*, for C4 and MMS, respectively. Red vertical lines in panels d and e and i and j mark the magnetosheath ion edge. For both C4 (Figure 4e) and MMS (Figure 4j) we observe magnetosheath electrons earthward of the MP with lower density but similar energy, deeper into the magnetosphere than magnetosheath ions, which suggest that reconnection is ongoing or was ongoing recently. This signature is attributed to a time of flight effect of electrons sitting on an open field line connected to the magnetosheath (Gosling et al., 1990; Vines et al., 2017). The eLLBL in Figure 4j cannot be distinguished at the time scale of the plot, please refer to Figure S7 in Supporting Information S1 of the supplemental material for a detailed observation of the eLLBL, which is not obvious for this event. The low energy electrons observed in Figure 4j after 17:49 UT are associated to cold ions of ionospheric origin (Figure 4j) and do not correspond to the eLLBL (e.g., Toledo-Redondo et al., 2021). We also search for jets in ion velocity (black lines in Figures 4c and 4h) of the order of the Alfvén velocity (listed in Table 3), which would indicate ongoing reconnection. For event 15, the data is not conclusive. Two possible narrow reconnection jets are observed at ∼17:48:45UT (Figure 4c, cluster) and ∼17:46:36 UT (Figure 4h, MMS), although their peak velocity in the *L* direction is less than 50% of the predicted Alfvén velocity. The blue-shaded regions correspond to the reference time interval (15 s) for inferring magnetosheath quantities, and the red-shaded regions correspond to the reference time interval (15 s) for inferring magnetospheric quantities. Ion velocities estimated by CIS-CODIF on C4 are not reliable in the magnetosphere due to the low counts, so they have been masked in panel c. We assume that velocity in the flank magnetosphere is negligible compared to flank magnetosheath velocity.

The same analysis explained in Figure 4 for event 15 has been applied to events 3, 5, 6, 8, 10 and 11, and their corresponding Figures are provided in Figures S1–S6 in Supporting Information S1. The reference magnetosheath and magnetosphere intervals adjacent to the MP crossings allow us to test the theoretical predictions of reconnection suppression by shear flows and the diamagnetic drift. The main parameters (*L*- and *N*-direction, magnetic field and density, hybrid Alfvén velocity, shear flow velocity, $\Delta\beta$ and **B** clock angle) are provided in Table S1 in Supporting Information S1. Table 3 summarizes the results of the expected reduction in reconnection rate due to shear flows, $(E/E_0)_{asym}$, whether reconnection is expected to be suppressed by the diamagnetic drift of the *X* line, and the observed reconnection signatures (jets and eLLBL).

4.1. Observational Evidence of Reconnection

The eLLBL is observed in all MMS crossings, although for event 15 the identification is ambiguous (see Figure S7 in Supporting Information S1), indicating that reconnection was taking place in the dayside region during the encounter. The eLLBL is also observed by C4 in the flank toward the end of the encounter, for events 11 and 15. This suggests that reconnection may be at work in the flank during the late hours of the encounter.

In addition, events 6, 10, and 11 show clear reconnection jets ($v_{jet} > 5v_A$) in the subsolar region (see Figures S3, S5, and S6 in Supporting Information S1), and possibly events 5, 8, and 15 ($v_{jet} < 0.5v_A$) (See Figure S2 and S4 in Supporting Information S1 and Figure 4). The direction of five of the jets (southward) is consistent with the expected location of the *X* line according to the maximum magnetic shear model (Trattner

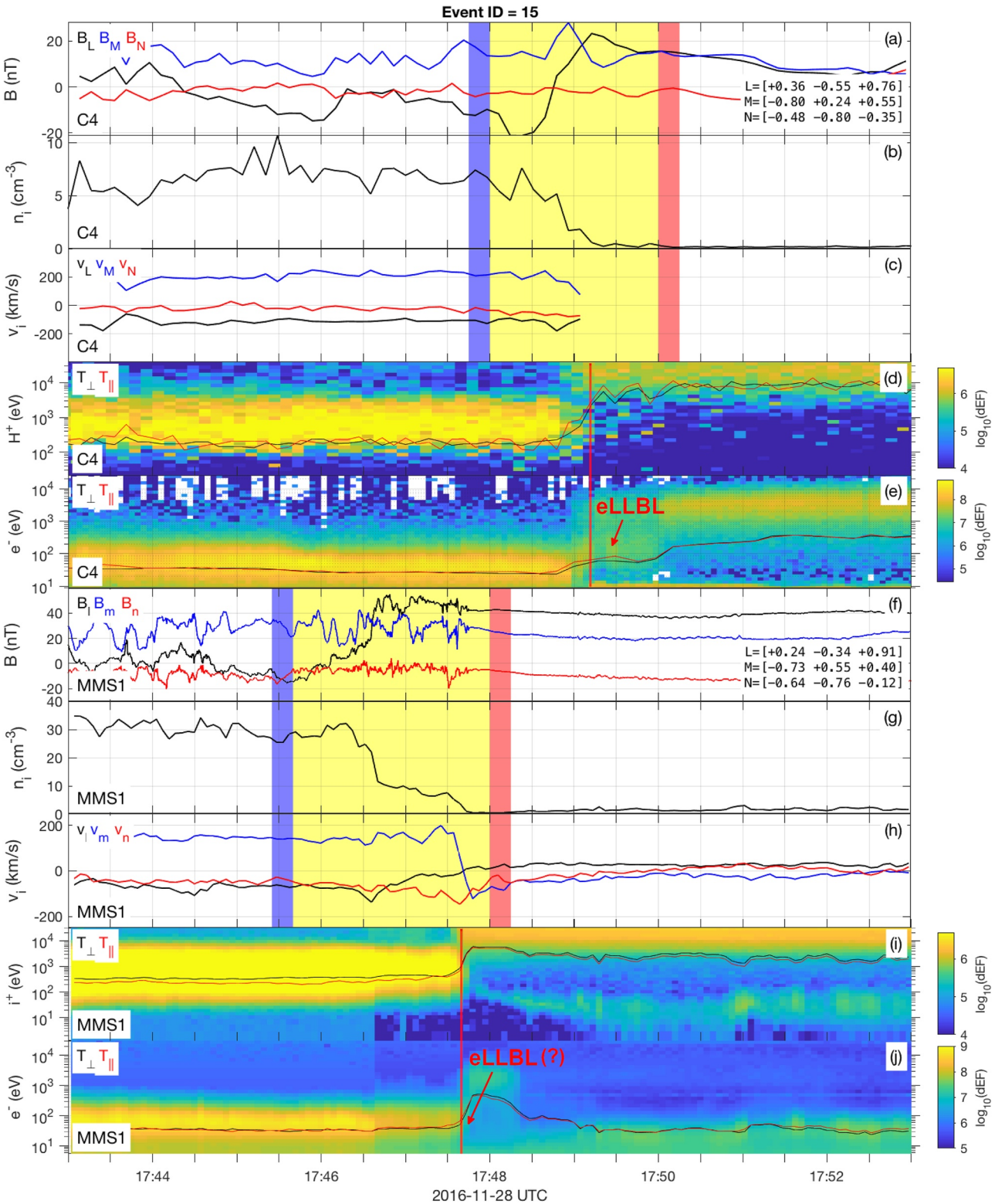
Event ID = 15
B (nT)
C4
L=[+0.36 −0.55 +0.76]
M=[−0.80 +0.24 +0.55]
N=[−0.48 −0.80 −0.35]
(a)
n_i (cm^-3)
(b)
v_i (km/s)
(c)
H+ (eV)
(d)
e- (eV)
(e)
eLLBL
log10(dEF)
MMS1
L=[+0.24 −0.34 +0.91]
M=[−0.73 +0.55 +0.40]
N=[−0.64 −0.76 −0.12]
(f)
(g)
(h)
i+ (eV)
(i)
eLLBL(?)
(j)
17:44
17:46
17:48
17:50
17:52
2016-11-28 UTC

Figure 4.

Table 3
Magnetic Reconnection Assessment at Dusk Flank (C4) and Subsolar Region (MMS)

ID	SC	L (GSE)	v_A[a] km/s)	$v_{s,L}$[b] (km/s)	$(E/E_0)_{asym}$[c]	Swisdak[d] prediction	Observed jet	e^- only LLBL
3	C4	−0.51 +0.27 −0.82	338	225	0.80	?	no	?
	MMS	+0.50 −0.28 +0.82	124	16	1.00	suppress	no	yes
5	C4	−0.82 +0.54 −0.16	146	262	0.71	suppress	no	?
	MMS	+0.11 +0.48 +0.87	249	15	1.00	suppress	? ($<0.5v_A$)	yes
6	C4	−0.78 +0.60 +0.16	221	248	0.95	suppress	no	no
	MMS	+0.50 −0.29 +0.82	188	1	1.00	?	yes ($>0.5v_A$)	yes
8	C4	−0.59 +0.50 +0.64	159	223	0.96	suppress	no	no
	MMS	+0.38 −0.45 +0.81	187	51	1.00	?	? ($<0.5v_A$)	yes
10	C4	+0.18 −0.41 +0.89	187	163	0.95	?	? ($<0.5v_A$)	?
	MMS	−0.05 −0.36 +0.93	169	100	0.98	?	yes ($>0.5v_A$)	yes
11	C4	−0.62 +0.33 +0.71	192	150	0.83	suppress	? ($<0.5v_A$)	yes
	MMS	+0.33 −0.53 +0.78	177	71	0.99	?	yes ($>0.5v_A$)	yes
15	C4	+0.36 −0.55 +0.76	228	116	0.98	allow	? ($<0.5v_A$)	yes
	MMS	+0.24 −0.34 +0.91	223	86	1.00	?	? ($<0.5v_A$)	yes(?)

Note. See Table S1 in Supporting Infromation S1 for additional information of the computed values.
[a]Hybrid Alfvén velocity (Cassak & Shay, 2007). [b]Shear flow speed parallel to the outflow (L) direction. [c]Expected reduction in reconnection rate due to shear flows, see Equation 3. [d]Diamagnetic drift of the X line, see Equation 4.

et al., 2007). Overall, the combination of eLLBL and jet identification suggests that reconnection was at work near the subsolar region during the whole encounter, while in the flank reconnection was at work after ∼13 UT. Clear jet signatures are not identified for all subsolar crossings, but this may be due to various reasons, including intermittent occurrence of reconnection, or the *X* line being close to the spacecraft position, as for the electron diffusion region event observed by MMS the same day at ∼07 UT (Genestreti et al., 2018).

4.2. Suppression of Magnetic Reconnection by Shear Flows

In the subsolar region (MMS observations), the *L* direction corresponds roughly to GSE *Z* for all the crossings, while the N direction is a combination of GSE *X* and GSE Y. On the other hand, the *L* direction is not stable in the dusk flank (C4 observations), with *L* changing between GSE -X and GSE Z. The N direction in the dusk flank is roughly in GSE Y and GSE *X*. Table 3 indicates that in the subsolar region, the observed shear flows in the *L* direction are smaller than the hybrid Alfvén velocity, resulting in negligible (less than 2%) expected reconnection rate reduction $(E/E_0)_{\text{asym}}$, according to Equation 3 (Doss et al., 2015). On the other hand, the shear flow velocity in the *L* direction is of the same order or larger than the hybrid Alfvén velocity in the dusk flank for all the events in Table 3, resulting in variable expected reconnection reductions, $0.71 < (E/E_0)_{\text{asym}} < 0.98$.

Figure 4. magnetospheric multiscale and cluster simultaneous observations of the MP during event 15 (see Table 1). The yellow-shaded regions mark the time interval used to apply minimum variance analysis to the current sheet crossing and obtain the LMN coordinate system for each spacecraft. Blue-shaded and red-shaded regions mark the intervals used as reference for the asymptotic conditions of the magnetosheath and the magnetosphere, respectively. (a) C4 magnetic field in LMN coordinates. (b) C4 ion number density. (c) C4 ion velocity in LMN coordinates. (d) (color) C4 CODIF proton spectrogram in differential Energy Flux units (dEF), keV/(cm^2 s sr keV) (black) perpendicular proton temperature (red) parallel proton temperature. (e) (color) C4 PEACE electron spectrogram in differential Energy Flux units (dEF), keV/(cm^2 s sr keV) (black) perpendicular electron temperature (red) parallel electron temperature. (f) MMS magnetic field in LMN coordinates. (g) MMS ion number density. (h) MMS ion velocity in LMN coordinates. (i) (color) MMS FPI ion spectrogram in differential Energy Flux units (dEF), keV/(cm^2 s sr keV) (black) perpendicular ion temperature (red) parallel ion temperature (j) (color) MMS FPI electron spectrogram in differential Energy Flux units (dEF), keV/(cm^2 s sr keV) (black) perpendicular electron temperature (red) parallel electron temperature.

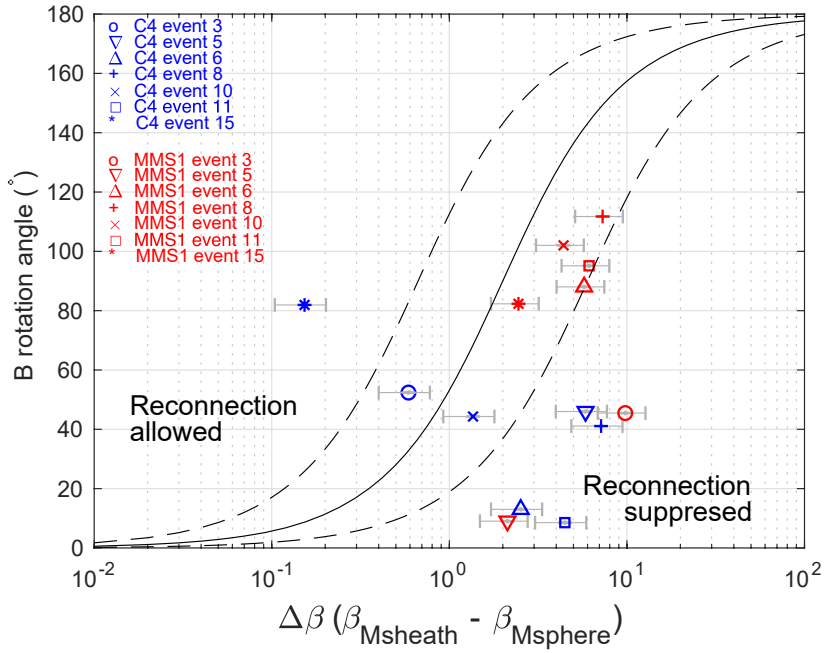

Figure 5. Local test of the diamagnetic drift reconnection suppression (Swisdak et al., 2003). Magnetic field clock angle in the LM plane versus corresponding change in plasma β across the MP current sheet ($\Delta\beta$), for all the crossings of Table 3. The solid line indicates $L/d_i = 1$, and the dashed lines indicate $L/d_i = 1/3$ and 3, see Equation 4.

4.3. Suppression of Magnetic Reconnection by Diamagnetic Drift

We test the Swisdak condition (Equation 4) at each MP crossing from Table 3, and plot the results in Figure 5. The black solid assumes $L/d_i = 1$, and the dashed lines assume $L/d_i = 1/3$ and $L/d_i = 3$. The plasma β in the magnetosheath and magnetosphere correspond to average values of 15 s intervals on each side of the MP current sheet (see Table S1 and Figures S1–S6 in Supporting Information S1). Their associated error bars correspond to the instrument uncertainties in measuring the plasma pressure, approximated by the channel energy widths of CODIF and FPI (16% and 15%, respectively). The uncertainty associated to the magnetic pressure measurement is less than 1%. The **B** rotation angle is taken in the plane perpendicular to the MP normal, i.e., the plane that contains L and M directions, computed using MVA on magnetic field data. The associated error in estimating the **B** rotation angle due to the magnetometers uncertainty is less than 1°. Uncertainty associated to the LMN coordinate system estimation can result in larger errors for the **B** rotation angle, but these are difficult to quantify.

We find that reconnection is expected to be suppressed for 6 of the crossings: 5, 6, 8 and 11 in the flank, and 3 and 5 in the subsolar region. In the flank, we did not identify reconnection signatures for crossings 5, 6, 8, therefore the theory is consistent with our observations for these crossings. For event 11 (blue square in Figure 5), however, we did observe the eLLBL plus a possible jet ($v < 0.5v_A$). In the subsolar region, event 3 (red circle in Figure 5) has eLLBL associated to it, and event 5 (red inverted triangle in Figure 5) has both eLLBL and a possible jet ($v < 0.5v_A$). We attribute this discrepancy with the theory to the fact that the Swisdak test is applied using plasma conditions at the spacecraft crossing, not at the X line location, which is unknown. These results suggest that the reconnection site was not close to Cluster for during event 11 and not close to MMS during events 3 and 5. The plasma β in the subsolar magnetosheath are most of the time well above 1 (red points in Figure 5). For reconnection to take place with such large magnetosheath plasma β, moderate to large **B** rotation angles are required (roughly larger than 90° for $\Delta\beta = 2$, see Figure 5). The clock angles and the $\Delta\beta$ are in general smaller in the flank (Cluster observations, blue) than in the subsolar magnetosphere (MMS observations, red).

5. Discussion and Conclusion

Park et al. (2016) analyzed 19 years of magnetospheric magnetic field data at geosynchronous orbit and cross-correlated it with magnetic field data of the solar wind at 1 AU. They found that for radial IMF conditions, the magnetospheric magnetic field was systematically smaller than for northward IMF conditions, over all magnetic local times and regardless of season or magnetic latitude. This result is consistent with the model of global expansion of the magnetosphere during radial IMF (Dusik et al., 2010). Our results in Figure 2 are consistent with an expansion of the order of 0.6–0.8 R_E near the subsolar region. At the flanks, we do not observe a deviation of the MP position predicted by the models S98 and L10, assuming an uncertainty of $\pm 0.2\ R_E$.

The persistent observation of the eLLBL in MMS data indicates that reconnection was at work in the subsolar region. This result is supported by the identification of reconnection jets in events 6, 10 and 11, and possibly in events 5, 8, and 15. By contrast, no jet signatures are present for event 3. The variability of jet observations has two possible explanations: MMS was close to the X line during some of the events, as for the event reported by Genestreti et al. (2018) few hours before, or reconnection was intermittent in time. Evidence for reconnection in the dusk flank is also present for events 11 and 15. This is consistent both with an X line extending from the MMS to the C4 location, i.e., more than 15 R_E, or with patchy reconnection involving multiple X lines. On the other hand, reconnection seems not to be at work in the flank MP near the C4 location for events 3, 5, 6, and 8.

While the L direction in the subsolar region is roughly in the GSE Z direction, in the flank is often oriented in the GSE X direction, i. e.., the direction of the magnetosheath flow. The predicted reconnection rate reductions due to shear flows in the flank are $E/E_0 = 2\%$ - 29% depending on the event, while the reconnection rate reduction is negligible (i.e., $E/E_0 < 2\%$) in the subsolar region. We note, however, that these calculations consider magnetosphere and magnetosheath references at the spacecraft location, while the conditions at the X line may be different, in particular the L direction.

During radial IMF conditions, the magnetosheath dynamic pressure becomes low, and the magnetic pressure that the magnetosheath exerts on the MP becomes even lower, resulting in an enhanced magnetosheath plasma β (e.g., Le & Russell, 1994; Suvorova et al., 2010; Suvorova & Dmitriev, 2016). The dynamic pressure in the magnetosheath is lower than in the solar wind during radial IMF owing to the quasi-parallel bow shock that is formed in the subsolar region and to the shorter size of the magnetosheath. The resulting magnetosheath β enhancement favors suppression of magnetic reconnection by the diamagnetic drift, as illustrated in Figure 5. However, these results are evaluated at the spacecraft location, not at the X line. In addition, accurate evaluation of Equation 4 requires reliable LMN coordinates. While the L direction determination is robust for our events, the N direction was less robust. The eigenvalue ratio of the intermediate to minimum direction (l_2/l_3) resulting from MVA was small (~3) for some of the events, which can result in errors in determining the effective **B** rotation angle across the MP. The magnetosheath magnetic field orientation and strength is variable during the encounter, as expected behind a quasi-parallel bow shock. Overall, radial IMF conditions may favor time-varying conditions at the MP, which may result in intermittent and spatial and time varying magnetic reconnection. More analysis of radial IMF events is needed to confirm these results.

To summarize, we analyzed an equatorial MP conjunction between MMS (subsolar region) and Cluster (dusk flank) during radial IMF conditions, enabling us to study the meso-scale of the MP using simultaneous in-situ measurements. Our results indicate that the magnetosphere inflates under radial IMF in the subsolar region (~0.7 R_E), while changes in the flank are <0.2 R_E, suggesting a MP deformation in addition to the inflation. Magnetic reconnection was at work in the subsolar region for the whole encounter based on the observed eLLBL, although reconnection jets were not always clearly identified. In the flank, reconnection was at work for the last hours of the encounter, suggesting that the extent of the X line could be larger than 15 R_E. However, the magnetosheath **B** is variable during radial IMF, and this may lead to patchy and non-steady magnetic reconnection at the MP.

Data Availability Statement

The omni database is publicly available at https://omniweb.gsfc.nasa.gov/. The MMS database is publicly available at https://lasp.colorado.edu/mms/sdc/public/. The Cluster database is publicly available at https://csa.esac.esa.int/.

Acknowledgments
S. Toledo-Redondo and J. Fornieles acknowledge support of the Ministry of Economy and Competitiveness (MINECO) of Spain (grant FIS2017-90102-R) and of Ministry of Science and Innovation (grant PID2020-112805GA-I00). Research at IRAP was supported by CNRS, CNES, and the University of Toulouse. We acknowledge support of the ISSI teams MMS and Cluster observations of magnetic reconnection and Cold plasma of ionospheric in the Earth's magnetosphere, and of the ESAC Science faculty.

References

Balogh, A., Dunlop, M., Cowley, S., Southwood, D., Thomlinson, J., Glassmeier, K., et al. (1997). The cluster magnetic field investigation. *Space Science Reviews*, *79*(1), 65–91. https://doi.org/10.1007/978-94-011-5666-0_3

Berchem, J., Marchaudon, A., Dunlop, M., Escoubet, C., Bosqued, J., Reme, H., & Carr, C. (2008). Reconnection at the dayside magnetopause: Comparisons of global MHD simulation results with cluster and double star observations. *Journal of Geophysical Research*, *113*(A7). https://doi.org/10.1029/2007ja012743

Boardsen, S., Eastman, T., Sotirelis, T., & Green, J. (2000). An empirical model of the high-latitude magnetopause. *Journal of Geophysical Research*, *105*(A10), 23193–23219. https://doi.org/10.1029/1998ja000143

Borovsky, J. E. (2008). The rudiments of a theory of solar wind/magnetosphere coupling derived from first principles. *Journal of Geophysical Research*, *113*(A8). https://doi.org/10.1029/2007ja012646

Borovsky, J. E., & Denton, M. H. (2006). Effect of plasmaspheric drainage plumes on solar-wind/magnetosphere coupling. *Geophysical Research Letters*, *33*(20). https://doi.org/10.1029/2006gl026519

Borovsky, J. E., Denton, M. H., Denton, R. E., Jordanova, V. K., & Krall, J. (2013). Estimating the effects of ionospheric plasma on solar wind/magnetosphere coupling via mass loading of dayside reconnection: Ion-plasma-sheet oxygen, plasmaspheric drainage plumes, and the plasma cloak. *Journal of Geophysical Research: Space Physics*, *118*(9), 5695–5719. https://doi.org/10.1002/jgra.50527

Burch, J. L., Moore, T. E., Torbert, R. B., & Giles, B. L. (2015). Magnetospheric multiscale overview and science objectives. *Space Science Reviews*, *199*(1–4), 5–21. https://doi.org/10.1007/s11214-015-0164-9

Case, N., & Wild, J. (2013). The location of the earth's magnetopause: A comparison of modeled position and in situ cluster data. *Journal of Geophysical Research: Space Physics*, *118*(10), 6127–6135. https://doi.org/10.1002/jgra.50572

Cassak, P. A., & Otto, A. (2011). Scaling of the magnetic reconnection rate with symmetric shear flow. *Physics of Plasmas*, *18*(7). https://doi.org/10.1063/1.3609771

Cassak, P. A., & Shay, M. A. (2007). Scaling of asymmetric magnetic reconnection: General theory and collisional simulations. *Physics of Plasmas*, *14*(10). https://doi.org/10.1063/1.2795630

Cowley, S., & Owen, C. (1989). A simple illustrative model of open flux tube motion over the dayside magnetopause. *Planetary and Space Science*, *37*(11), 1461–1475. https://doi.org/10.1016/0032-0633(89)90116-5

Dargent, J., Aunai, N., Lavraud, B., Toledo-Redondo, S., & Califano, F. (2020). Simulation of plasmaspheric plume impact on dayside magnetic reconnection. *Geophysical Research Letters*, *47*(4), e2019GL086546. https://doi.org/10.1029/2019gl086546

Desroche, M., Bagenal, F., Delamere, P. A., & Erkaev, N. (2013). Conditions at the magnetopause of saturn and implications for the solar wind interaction. *Journal of Geophysical Research: Space Physics*, *118*(6), 3087–3095. https://doi.org/10.1002/jgra.50294

Doss, C., Cassak, P., & Swisdak, M. (2016). Particle-in-cell simulation study of the scaling of asymmetric magnetic reconnection with in-plane flow shear. *Physics of Plasmas*, *23*(8), 082107. https://doi.org/10.1063/1.4960324

Doss, C. E., Komar, C. M., Cassak, P. A., Wilder, F. D., Eriksson, S., & Drake, J. F. (2015). Asymmetric magnetic reconnection with a flow shear and applications to the magnetopause. *Journal of Geophysical Research: Space Physics*, *120*(9), 7748–7763. https://doi.org/10.1002/2015ja021489

Dunlop, M. W., Zhang, Q. H., Bogdanova, Y. V., Lockwood, M., Pu, Z., Hasegawa, H., & Liu, Z. X. (2011). Extended magnetic reconnection across the dayside magnetopause. *Physical Review Letters*, *107*(2), 025004. https://doi.org/10.1103/physrevlett.107.025004

Dusik, S., Granko, G., Safrankova, J., Nemecek, Z., & Jelinek, K. (2010). IMF cone angle control of the magnetopause location: Statistical study. *Geophysical Research Letters*, *37*(19).

Escoubet, C. P., Fehringer, M., & Goldstein, M. (2001). The cluster mission - Introduction. *Annales Geophysicae*, *19*(10–12), 1197–1200. https://doi.org/10.5194/angeo-19-1197-2001

Fairfield, D., Baumjohann, W., Paschmann, G., Lühr, H., & Sibeck, D. (1990). Upstream pressure variations associated with the bow shock and their effects on the magnetosphere. *Journal of Geophysical Research*, *95*(A4), 3773–3786. https://doi.org/10.1029/ja095ia04p03773

Fairfield, D. H. (1971). Average and unusual locations of the earth's magnetopause and bow shock. *Journal of Geophysical Research*, *76*(28), 6700–6716. https://doi.org/10.1029/ja076i028p06700

Fear, R. C., Milan, S. E., Fazakerley, A. N., Fornaçon, K. H., Carr, C. M., & Dandouras, I. (2009). Simultaneous observations of flux transfer events by themis, cluster, double star, and superdarn: Acceleration of ftes. *Journal of Geophysical Research*, *114*(A10). https://doi.org/10.1029/2009ja014310

Fuselier, S., Petrinec, S., Sawyer, R., Mukherjee, J., & Masters, A. (2020). Suppression of magnetic reconnection at saturn's low-latitude magnetopause. *Journal of Geophysical Research: Space Physics*, *125*(5), e2020JA027895. https://doi.org/10.1029/2020ja027895

Fuselier, S. A., Burch, J. L., Mukherjee, J., Genestreti, K. J., Vines, S. K., Gomez, R., et al. (2017). Magnetospheric ion influence at the dayside magnetopause. *Journal of Geophysical Research: Space Physics*, *122*(8), 8617–8631. https://doi.org/10.1002/2017ja024515

Fuselier, S. A., Haaland, S., Tenfjord, P., Paschmann, G., Toledo-Redondo, S., Malaspina, D., & Giles, B. L. (2021). High-density magnetospheric he+ at the dayside magnetopause and its effect on magnetic reconnection. *Journal of Geophysical Research: Space Physics*, *126*(1). https://doi.org/10.1029/2020ja028722

Fuselier, S. A., Mukherjee, J., Denton, M. H., Petrinec, S. M., Trattner, K. J., Toledo-Redondo, S., et al. (2019). High-density o+ in earth's outer magnetosphere and its effect on dayside magnetopause magnetic reconnection. *Journal of Geophysical Research: Space Physics*, *124*(12), 10257–10269. https://doi.org/10.1029/2019ja027396

Fuselier, S. A., Trattner, K. J., Petrinec, S. M., Denton, M. H., Toledo-Redondo, S., André, M., et al. (2019). Mass loading the earth's dayside magnetopause boundary layer and its effect on magnetic reconnection. *Geophysical Research Letters*, *46*(12), 6204–6213. https://doi.org/10.1029/2019gl082384

Genestreti, K. J., Varsani, A., Burch, J. L., Cassak, P. A., Torbert, R. B., Nakamura, R., & Baumjohann, W. (2018). Mms observation of asymmetric reconnection supported by 3-d electron pressure divergence. *Journal of Geophysical Research: Space Physics*. https://doi.org/10.1002/2017ja025019

Gosling, J. T., Thomsen, M. F., Bame, S. J., Onsager, T. G., & Russell, C. T. (1990). The electron edge of low latitude boundary layer during accelerated flow events. *Geophysical Research Letters*, *17*(11), 1833–1836. https://doi.org/10.1029/gl017i011p01833

Kitamura, N., Hasegawa, H., Saito, Y., Shinohara, I., Yokota, S., Nagai, T., et al. (2016). Shift of the magnetopause reconnection line to the winter hemisphere under southward IMF conditions: Geotail and mms observations. *Geophysical Research Letters*, *43*(11), 5581–5588. https://doi.org/10.1002/2016gl069095

La Belle-Hamer, A., Otto, A., & Lee, L. (1995). Magnetic reconnection in the presence of sheared flow and density asymmetry: Applications to the earth's magnetopause. *Journal of Geophysical Research*, *100*(A7), 11875–11889. https://doi.org/10.1029/94ja00969

Lavraud, B., & Borovsky, J. E. (2008). Altered solar wind-magnetosphere interaction at low mach numbers: Coronal mass ejections. *Journal of Geophysical Research*, *113*(A9). https://doi.org/10.1029/2008ja013192

Le, G., & Russell, C. (1994). The thickness and structure of high beta magnetopause current layer. *Geophysical Research Letters*, *21*(23), 2451–2454. https://doi.org/10.1029/94gl02292

Lin, R. L., Zhang, X. X., Liu, S. Q., Wang, Y. L., & Gong, J. C. (2010). A three-dimensional asymmetric magnetopause model. *Journal of Geophysical Research*, *115*(A4). https://doi.org/10.1029/2009ja014235

Lu, J., Liu, Z., Kabin, K., Jing, H., Zhao, M., & Wang, Y. (2013). The IMF dependence of the magnetopause from global MHD simulations. *Journal of Geophysical Research: Space Physics*, *118*(6), 3113–3125. https://doi.org/10.1002/jgra.50324

Lu, J., Liu, Z., Kabin, K., Zhao, M., Liu, D., Zhou, Q., & Xiao, Y. (2011). Three dimensional shape of the magnetopause: Global mhd results. *Journal of Geophysical Research*, *116*(A9). https://doi.org/10.1029/2010ja016418

Marchaudon, A., Owen, C., Bosqued, J.-M., Fear, R., Fazakerley, A., Dunlop, M., et al. (2005). Simultaneous double star and cluster ftes observations on the dawnside flank of the magnetosphere. *Annales Geophysicae*, *23*, 2877–2887. https://doi.org/10.5194/angeo-23-2877-2005

McComas, D., Bame, S., Barker, P., Feldman, W., Phillips, J., Riley, P., & Griffee, J. (1998). Solar wind electron proton alpha monitor (SWEPAM) for the advanced composition explorer. *The Advanced Composition Explorer Mission*, 563–612. https://doi.org/10.1007/978-94-011-4762-0_20

Merka, J., Szabo, A., Šafránková, J., & Němeček, Z. (2003). Earth's bow shock and magnetopause in the case of a field-aligned upstream flow: Observation and model comparison. *Journal of Geophysical Research*, *108*(A7). https://doi.org/10.1029/2002ja009697

Palmroth, M., Janhunen, P., Pulkkinen, T., & Peterson, W. (2001). Cusp and magnetopause locations in global mhd simulation. *Journal of Geophysical Research*, *106*(A12), 29435–29450. https://doi.org/10.1029/2001ja900132

Park, J., Shue, J., Kim, K., Pi, G., Němeček, Z., & Šafránková, J. (2016). Global expansion of the dayside magnetopause for long-duration radial IMF events: Statistical study on goes observations. *Journal of Geophysical Research: Space Physics*, *121*(7), 6480–6492. https://doi.org/10.1002/2016ja022772

Petrinec, S., & Russell, C. (1996). Near-earth magnetotail shape and size as determined from the magnetopause flaring angle. *Journal of Geophysical Research*, *101*(A1), 137–152. https://doi.org/10.1029/95ja02834

Phan, T., Hasegawa, H., Fujimoto, M., Oieroset, M., Mukai, T., Lin, R., & Paterson, W. (2006). Simultaneous geotail and wind observations of reconnection at the subsolar and tail flank magnetopause. *Geophysical Research Letters*, *33*(9). https://doi.org/10.1029/2006gl025756

Phan, T., Kistler, L., Klecker, B., Haerendel, G., Paschmann, G., Sonnerup, B. O., et al. (2000). Extended magnetic reconnection at the earth's magnetopause from detection of bi-directional jets. *Nature*, *404*(6780), 848–850. https://doi.org/10.1038/35009050

Phan, T., Paschmann, G., Gosling, J., Oieroset, M., Fujimoto, M., Drake, J., & Angelopoulos, V. (2013). The dependence of magnetic reconnection on plasma beta and magnetic shear: Evidence from magnetopause observations. *Geophysical Research Letters*, *40*(1), 11–16. https://doi.org/10.1029/2012gl054528

Pi, G., Shue, J., Chao, J., Němeček, Z., Šafránková, J., & Lin, C. (2014). A reexamination of long-duration radial imf events. *Journal of Geophysical Research*, *119*(9), 7005–7011. https://doi.org/10.1002/2014ja019993

Pollock, C., Moore, T., Jacques, A., Burch, J., Gliese, U., Saito, Y., & Zeuch, M. (2016). Fast plasma investigation for magnetospheric multiscale. *Space Science Reviews*, *199*(1–4), 331–406. https://doi.org/10.1007/s11214-016-0245-4

Reme, H., Aoustin, C., Bosqued, J., Dandouras, I., Lavraud, B., Sauvaud, J., et al. (2001). First multispacecraft ion measurements in and near the earth's magnetosphere with the identical cluster ion spectrometry (cis) experiment. *Annales Geophysicae*, *19*, 1303–1354. https://doi.org/10.5194/angeo-19-1303-2001

Russell, C. T., Anderson, B. J., Baumjohann, W., Bromund, K. R., Dearborn, D., Fischer, D., & Richter, I. (2014). The magnetospheric multiscale magnetometers. *Space Science Reviews*, *199*(1–4), 189–256. https://doi.org/10.1007/s11214-014-0057-3

Safrankova, J., Nemecek, Z., Dusik, S., Prech, L., Sibeck, D., & Borodkova, N. (2002). The magnetopause shape and location: A comparison of the interball and geotail observations with models. *Annales Geophysicae*, *20*, 301–309.

Samsonov, A. A., Gordeev, E., Tsyganenko, N. A., Šafránková, J., Němeček, Z., Šimůnek, J., et al. (2016). Do we know the actual magnetopause position for typical solar wind conditions? *Journal of Geophysical Research: Space Physics*, *121*(7), 6493–6508. https://doi.org/10.1002/2016ja022471

Samsonov, A. A., Němeček, Z., Šafránková, J., & Jelínek, K. (2012). Why does the subsolar magnetopause move sunward for radial interplanetary magnetic field? *Journal of Geophysical Research*, *117*(A5), n/a–n. https://doi.org/10.1029/2011ja017429

Sawyer, R., Fuselier, S., Mukherjee, J., & Petrinec, S. (2019). An investigation of flow shear and diamagnetic drift effects on magnetic reconnection at saturn's dawnside magnetopause. *Journal of Geophysical Research: Space Physics*, *124*(11), 8457–8473. https://doi.org/10.1029/2019ja026696

Shue, J., Song, P., Russell, C., Steinberg, J., Chao, J., Zastenker, G., et al. (1998). Magnetopause location under extreme solar wind conditions. *Journal of Geophysical Research*, *103*(A8), 17691–17700. https://doi.org/10.1029/98ja01103

Sibeck, D. G., Lopez, R., & Roelof, E. C. (1991). Solar wind control of the magnetopause shape, location, and motion. *Journal of Geophysical Research*, *96*(A4), 5489–5495. https://doi.org/10.1029/90ja02464

Smith, C. W., L'Heureux, J., Ness, N. F., Acuna, M. H., Burlaga, L. F., & Scheifele, J. (1998). The Ace Magnetic Fields Experiment. *The advanced composition explorer mission* (pp. 613–632). https://doi.org/10.1007/978-94-011-4762-0_21

Suvorova, A., & Dmitriev, A. (2015). Magnetopause inflation under radial IMF: Comparison of models. *Earth and Space Science*, *2*(4), 107–114. https://doi.org/10.1002/2014ea000084

Suvorova, A., & Dmitriev, A. (2016). On magnetopause inflation under radial IMF. *Advances in Space Research*, *58*(2), 249–256. https://doi.org/10.1016/j.asr.2015.07.044

Suvorova, A., Shue, J., Dmitriev, A., Sibeck, D., McFadden, J., Hasegawa, H., & Němeček, Z. (2010). Magnetopause expansions for quasi-radial interplanetary magnetic field: Themis and geotail observations. *Journal of Geophysical Research*, *115*(A10). https://doi.org/10.1029/2010ja015404

Swisdak, M., Opher, M., Drake, J., & Bibi, F. A. (2010). The vector direction of the interstellar magnetic field outside the heliosphere. *The Astrophysical Journal*, *710*(2), 1769–1775. https://doi.org/10.1088/0004-637x/710/2/1769

Swisdak, M., Rogers, B., Drake, J., & Shay, M. (2003). Diamagnetic suppression of component magnetic reconnection at the magnetopause. *Journal of Geophysical Research*, *108*(A5). https://doi.org/10.1029/2002ja009726

Toledo-Redondo, S., André, M., Aunai, N., Chappell, C. R., Dargent, J., Fuselier, S. A., & Vines, S. K. (2021). Impacts of ionospheric ions on magnetic reconnection and earth's magnetosphere dynamics. *Reviews of Geophysics*, *59*(3), e2020RG000707. https://doi.org/10.1029/2020RG000707

Trattner, K., Mulcock, J., Petrinec, S., & Fuselier, S. (2007). Probing the boundary between antiparallel and component reconnection during southward interplanetary magnetic field conditions. *Journal of Geophysical Research*, *112*(A8). https://doi.org/10.1029/2007ja012270

Vernisse, Y., Lavraud, B., Faganello, M., Fadanelli, S., Sisti, M., Califano, F., & Pollock, C. (2020). Latitudinal dependence of the kelvin-helmholtz instability and beta dependence of vortex-induced high-guide field magnetic reconnection. *Journal of Geophysical Research*, *125*(5), e2019JA027333. https://doi.org/10.1029/2019ja027333

Vines, S. K., Fuselier, S. A., Trattner, K. J., Burch, J. L., Allen, R. C., Petrinec, S. M., et al. (2017). Magnetospheric ion evolution across the low-latitude boundary layer separatrix. *Journal of Geophysical Research: Space Physics*, *122*(1010), 247262–247310. https://doi.org/10.1002/2017ja024061

Walsh, B. M., Komar, C. M., & Pfau-Kempf, Y. (2017). Spacecraft measurements constraining the spatial extent of a magnetopause reconnection x line. *Geophysical Research Letters*, *44*(7), 3038–3046. https://doi.org/10.1002/2017gl073379

Walsh, B. M., Sibeck, D. G., Nishimura, Y., & Angelopoulos, V. (2013). Statistical analysis of the plasmaspheric plume at the magnetopause. *Journal of Geophysical Research: Space Physics*, *118*(8), 4844–4851. https://doi.org/10.1002/jgra.50458

Wang, Y., Sibeck, D., Merka, J., Boardsen, S., Karimabadi, H., Sipes, T., et al. (2013). A new three-dimensional magnetopause model with a support vector regression machine and a large database of multiple spacecraft observations. *Journal of Geophysical Research: Space Physics*, *118*(5), 2173–2184. https://doi.org/10.1002/jgra.50226

Wiltberger, M., Lopez, R., & Lyon, J. (2003). Magnetopause erosion: A global view from MHD simulation. *Journal of Geophysical Research*, *108*(A6). https://doi.org/10.1029/2002ja009564